Article

Dendrite-Free Zn Anode Modified by Organic Coating for Stable Aqueous Zinc Ion Batteries

Fujie Li, Hongfei Zhang, Xuehua Liu, Binghui Xu [ID] and Chao Wang *[ID]

Institute of Materials for Energy and Environment, College of Materials Science and Engineering, Qingdao University, Qingdao 266071, China
*   Correspondence: wangc@qdu.edu.cn

Abstract: Aqueous zinc-ion batteries (AZIBs) have emerged as highly promising options for large-scale energy storage systems due to their cost-effectiveness, substantial energy capacity, and improved safety features. However, the Zn anode faces challenges such as self-corrosion and dendrite formation, which limit its practical use in AZIB applications. In this work, a simple blade-coating method was used to successfully coat poly (vinylidene fluoride–hexafluoro propylene) (PVDF-HFP) on the Zn anode. The coated Zn anode (P-Zn) displayed a stable cycling performance (700 h) at 1 mA cm^{-2} current density in the symmetric cell. In addition, the full cell using MnO_2 as the cathode and P-Zn as the anode retained almost full capacity even after 1400 cycles at 2C, far outperforming the full cell using the unmodified Zn anode with only 50% capacity retention after 600 cycles. In situ optical observations of Zn deposition demonstrate that the special organic coating significantly enhances the uniform deposition of Zn^{2+}, thus effectively mitigating corrosion and hydrogen evolution. Density Functional Theory (DFT) calculations show that the PVDF-HFP coating effectively narrows the adsorption energy gap between the P-Zn (002) and (101) planes, leading to the homogeneous deposition of Zn^{2+} with fewer Zn dendrites. A simple and feasible strategy for designing ultra-stable AZIBs by coating an organic protective layer on the Zn surface is provided by this work.

Keywords: aqueous zinc ion battery; organic coating; zinc dendrites; long cycling stability

1. Introduction

Rechargeable aqueous zinc ion batteries (AZIBs) have become a popular research target in recent years as a candidate for large-scale energy storage devices with low cost, high safety, and environmental friendliness [1–4]. Owing to the advantages of abundant reserves, low redox potential (−0.76 V vs. SHE), and ultra-high theoretical volumetric energy density (5851 mAh cm^3), AZIBs usually directly use pure metallic Zn foil as the anode [5,6].

In AZIBs, the cycling stability of the Zn anode is a significant challenge due to the interplay of complex electrochemical and chemical processes [7,8]. One of the primary issues is the growth of Zn dendrites, which occurs during the deposition of Zn^{2+} on the anode surface. These dendrites not only increase the electrode surface area but also penetrate the separator, leading to the potential short-circuiting of the battery [9]. Additionally, due to the low standard electrode potential of Zn, the electrode may reach the threshold for the hydrogen evolution reaction (HER), resulting in hydrogen gas generation [10]. The evolution of hydrogen gas further accelerates electrolyte consumption. Moreover, the Zn dissolution and redeposition processes are often non-uniform due to uneven current density distribution, which leads to unstable electrode structures and deteriorated electrochemical performance [11]. Beyond these electrochemical reactions, the Zn anode is also susceptible to chemical corrosion, which is exacerbated by the increased contact area between the electrode and the electrolyte, particularly after dendrite growth [6,12]. Furthermore, the formation of insulating by-products like $Zn_4SO_4(OH)_6 \cdot 5H_2O$ (ZSH) on

the anode surface contributes to a passivation layer that impedes uniform zinc deposition, ultimately impairing the redox kinetics and cycling stability [13,14].

The aforementioned issues pertaining to the Zn anode have been addressed through the implementation of various strategies, including structural construction [15,16], electrolyte optimization [17–19], surface modification [20,21], and Zn alloy preparation [22,23]. Various surface modification techniques have been extensively investigated to enhance the electrode–electrolyte interface using different coatings to improve the performance [24–27]. For example, the Zn anode modified with a metal–organic framework coating showed an 88.9% high-capacity retention after 600 cycles. This coating helps to form a supersaturated surface with low interfacial resistance [28]. Hu et al. utilized a simple drop-coating approach to cover the Zn anode with polyacrylonitrile (PAN), which led to a more uniform Zn^{2+} deposition and enhanced cycling durability [29]. Likewise, Cui et al. demonstrated that polyamide (PA) coatings, known for their robust coordination with Zn^{2+} and unique hydrogen bonding networks, contribute positively to the performance of Zn electrodes [30]. Notably, a PA-coated Zn anode exhibited a stable current over 8000 h of cycling without the formation of Zn dendrites, highlighting its potential to improve electrode stability.

In this study, we successfully applied a poly(vinylidene fluoride–hexafluoropropylene) (PVDF-HFP) coating on the Zn anode using a simple blade-coating method. The objective was to enhance the long-term cycling stability of the Zn anode by reducing Zn dendrite formation. The modified Zn anode (P-Zn) symmetric cell demonstrated stable Coulombic efficiency and an impressive cycling life of 700 h at 1 mA cm^{-2} current density. Moreover, the full cell configured with MnO_2 as the cathode and P-Zn as the anode demonstrated remarkable stability, maintaining its full capacity even after 1400 cycles at 2C. In comparison, the full cell utilizing an uncoated Zn anode maintained only 50% of its original capacity after just 600 cycles, highlighting the significant improvement in performance due to the P-Zn modification. The PVDF-HFP coating effectively reduces the adsorption energy difference between the P-Zn (002) and (101) planes, as predicted by the Density Functional Theory (DFT), leading to uniform Zn^{2+} deposition and fewer Zn dendrites. This results in reduced corrosion and fewer by-products, improving the reversibility of the Zn^{2+}/Zn stripping/plating process. This straightforward approach of applying an organic coating to the Zn anode presents a promising solution for developing AZIBs with enhanced stability and dendrite-free performance.

2. Materials and Synthesis

Materials. All reagents were utilized as provided without further purification. This included Zn foil sourced from Aladdin (Aladdin Biochemical Technology Co., Ltd., Shanghai, China), concentrated H_2SO_4 (95–98%) from Sinopharm Chemical Reagent (Sinopharm Chemical Reagent Co., Ltd., Shanghai, China), as well as $MnSO_4 \cdot H_2O$, $ZnSO_4$, and MnO_2, all obtained from Aladdin (Aladdin Biochemical Technology Co., Ltd., Shanghai, China). Additional chemicals like poly(vinylidene fluoride–hexafluoropropylene) (PVDF-HFP) from Solvay (Solvay (Shanghai) Co., Ltd., Shanghai, China), conductive carbon (Super P, Timcal Super C65), and N-methyl-2-pyrrolidone (NMP) from Aladdin (Aladdin Biochemical Technology Co., Ltd., Shanghai, China) were also employed.

Preparation of P-Zn. The PVDF-HFP film was applied onto the Zn surface using a straightforward blade-coating technique. Initially, 50 mg of PVDF-HFP was dissolved in 4 mL of NMP to create a uniform solution. This solution was then spread over the Zn foil using a scraper blade with a 100 μm thickness. The Zn sample with the coating was then vacuum-dried at 60 °C for a duration of 12 h, yielding the modified version referred to as P-Zn. For the comparison, two additional samples were prepared using the same method but with 25 mg and 75 mg of PVDF-HFP, referred to as P-Zn25 and P-Zn75, respectively.

3. Results and Discussion

Figure 1a presents a comparative analysis of the X-ray diffraction (XRD) patterns of the bare Zn and P-Zn samples. The Zn and P-Zn diffraction peaks are in accordance with

the standard card (PDF # 04-0831), and no significant variations were observed in the peak positions and intensities for both samples [31,32]. This was due to the thin PVDF-HFP layer, which did not affect the crystal structure of zinc metal. The high-resolution F 1s X-ray photoelectron spectroscopy (XPS) spectrum of P-Zn is shown in Figure 1b. There is a characteristic peak at 686.2 eV, corresponding to the F 1s of the PVDF-HFP coating layer [31,33].
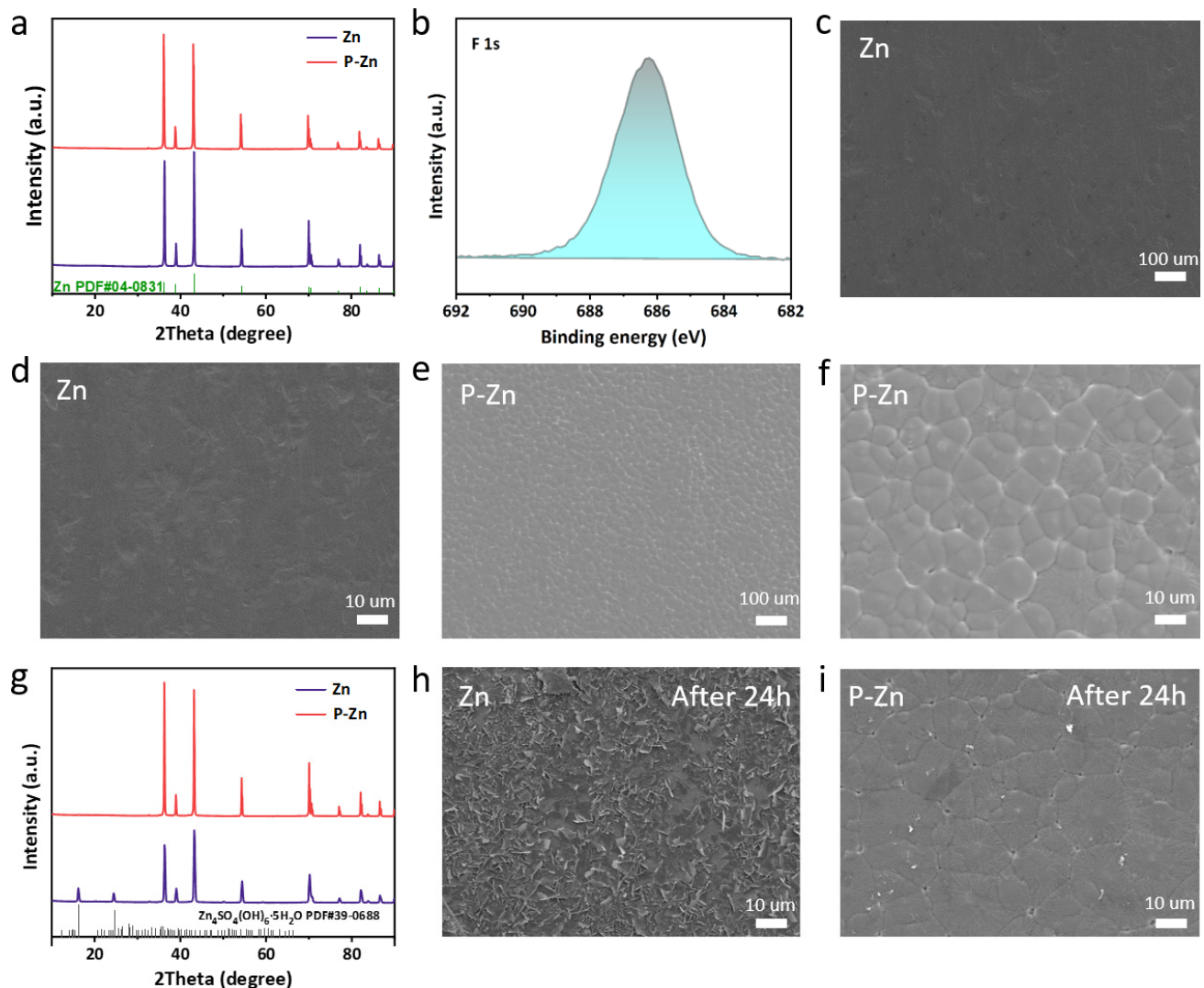

Figure 1. Characterization results: (**a**) XRD patterns comparing Zn and P-Zn. (**b**) High-resolution XPS spectrum for the F 1s region of P-Zn. (**c**,**d**) FESEM images showing the surface morphology of bare Zn and (**e**,**f**) FESEM images of P-Zn. (**g**) XRD patterns of both bare Zn and P-Zn after 24 h of immersion. (**h**,**i**) FESEM images depicting surface changes in bare Zn and P-Zn post 24 h of immersion.

Figure 1c–f present field-emission scanning electron microscopy (FESEM) images for uncoated Zn and P-Zn, respectively. In contrast to the bare Zn, which shows a smooth surface, the P-Zn sample reveals a dense PVDF-HFP coating layer. The dense surface structure effectively isolates the Zn anode from the aqueous electrolyte, thereby reducing the risk of self-corrosion and hydrogen evolution [20]. Figure S1 shows the cross-sectional FESEM image of P-Zn. It can be observed that the thickness of the coating layer is about 10 μm. Figures S2 and S3 present the FESEM images of P-Zn25 and P-Zn75 samples, respectively. It was found that a low concentration of PVDF-HFP resulted in the non-uniform distribution of the coating (Figure S2), while a too-high concentration resulted in an excessively thick coating, which is unfavorable for the transport of Zn^{2+} (Figure S3).

In order to more clearly assess the corrosion resistance of the Zn and P-Zn samples, they were placed in a concentrated $ZnSO_4$ solution for 24 h. Figure 1g presents the XRD patterns of the two samples following 24 h of immersion. The diffraction peaks corresponding to the by-products ZSH (PDF # 39-0688) were observed in the bare Zn sample, with a noticeable decrease in peak intensity [31]. This indicates that an active interfacial reaction occurred, and the corrosion by-product covered the surface of the Zn anode. In contrast, the XRD pattern of P-Zn remained unaltered, thereby corroborating the positive impact of the PVDF-HFP coating in impeding the generation of by-products. Figure 1h,i show the FESEM images of bare Zn and P-Zn after being immersed in a $ZnSO_4$ solution for 24 h, respectively. The bare Zn surface is filled with corrosion by-product deposits, which are usually responsible for low redox kinetics and the poor cycling stability of the Zn anode. However, the surface of P-Zn still remains intact with a dense morphology without any noticeable changes. This proves that the PVDF-HFP coating is beneficial in reducing the corrosion and the generation of the ZSH by-product, thus improving the reversibility of Zn^{2+}/Zn stripping/plating [21]. The FESEM image of P-Zn25 after immersion in $ZnSO_4$ solution for 24 h is shown in Figure S4. It can be observed that the areas covered by the PVDF-HFP coating in P-Zn25 remain intact, while the uncovered areas corrode completely, forming corrosion by-products. This further confirms the positive role of the PVDF-HFP coating in inhibiting the by-product's generation.

Figure 2a shows the Tafel curves of Zn and P-Zn electrodes in a 2 M Zn_2SO_4 aqueous electrolyte. It can be observed that the corrosion potential of the P-Zn electrode is -0.97 V, which is larger than that of the Zn electrode (-0.99 V). This indicates that the PVDF-HFP coating of the P-Zn electrode leads to the alleviation of the corrosion reaction [34]. In the Linear sweep voltammetry (LSV) test (Figure 2b), the P-Zn electrode exhibits a lower potential of -1.51 V than that of the Zn electrode (-1.36 V) at the same current density. This demonstrates that the PVDF coating layer of P-Zn is beneficial for the reduced HER, which inhibits the ZSH by-products [34].

Coulombic efficiency is a key factor in order to evaluate the stability and lifespan of the battery [35]. As shown in Figure 2c, half cells were assembled using bare Zn and P-Zn electrodes with pure Cu foil and were tested for long-cycle performance at a current density of 1 mA cm^{-2}. The Zn||Cu half-cell demonstrated irregular Coulombic efficiency after reaching 300 cycles. This deterioration can be attributed to the short circuit caused by the inhomogeneous deposition of Zn^{2+} on the surface of the bare Zn electrode. In contrast, the P-Zn||Cu half-cell can be stably cycled for about 1500 cycles with the Coulombic efficiency maintained at 100%, which highlights the commendable stability possessed by the PVDF-HFP coating. Figure 2d illustrates the Galvanostatic cycling profiles for both Zn||Cu and P-Zn||Cu half-cells. The data indicate that the P-Zn electrode shows reduced polarization voltage within the same voltage window in comparison to the bare Zn electrode, which contributes to its improved stability [18].

Figure 2e shows the long-term stability of Zn||Zn and P-Zn||P-Zn symmetric cells at a current density of 1 mA cm^{-2} to evaluate the effect of the PVDF-HFP coating on cell performance. The results show that the bare Zn electrode has a large polarization voltage and suddenly fails after about 100 h of cycling, which is caused by the formation of Zn dendrites during the Zn^{2+} stripping/plating process, leading to a short circuit [36]. On the other hand, the P-Zn||P-Zn symmetric cell maintains a steady polarization voltage with only a slight increase over 700 h, indicating a highly reversible Zn^{2+}/Zn stripping and plating process. Figure 2f compares the rate of performance of the symmetric cells. The polarization voltage of the bare Zn electrode is consistently larger as the current increases, and the bare Zn electrode short circuits and fails when the current reaches 5 mA cm^{-2}. However, the P-Zn electrode shows an excellent rate of performance and a relatively stable voltage without significant polarization. These tests consistently emphasize the excellent and stable performance of the PVDF-HFP coating in terms of Zn^{2+} stripping/plating, which greatly extends the lifespan of the cell.
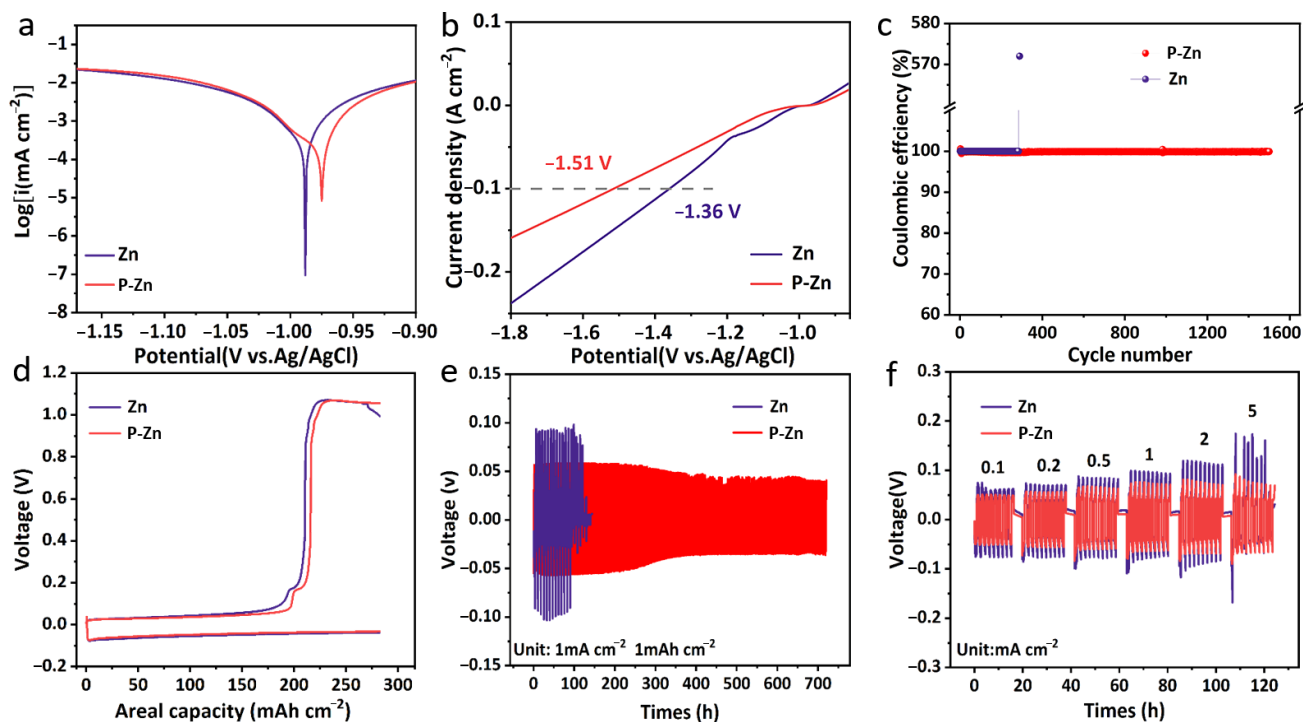
Figure 2. (**a**) Tafel corrosion curves and (**b**) LSV curves of bare Zn and P-Zn electrodes in the 2 M Zn_2SO_4 aqueous electrolyte at the scan rate of 5 mV s^{-1}. (**c**) Coulombic efficiencies of bare Zn and P-Zn stripping/plating on Cu foil at 1 mA cm^{-2}. (**d**) Galvano static cycling curves on Cu foil at 1 mA cm^{-2}. (**e**) Long-term stability of Zn||Zn and P-Zn||P-Zn symmetric cells at 1 mA cm^{-2}. (**f**) The rate of performance of Zn||Zn and P-Zn||P-Zn symmetric cells evaluated across various current densities ranging from 0.1 to 5 mA cm^{-2}.

The dendrite growth behavior of bare Zn and P-Zn electrodes was carefully investigated using in situ optical microscopy, as shown in Figure 3. It was noticeable that irregular dendrites started to appear on the surface of the bare Zn electrode after just 20 min at a current density of 10 mA cm^{-2} (Figure 3a). By 40 min, these dendrites rapidly expanded to form a distinct network. By 60 min, the surface of the bare Zn electrode was almost completely covered by a dense network of irregular dendrites, which could easily lead to a short circuit of the battery, seriously affecting its stability and lifespan. In contrast, the P-Zn electrode was very stable throughout the process, with no significant dendrite growth on the surface (Figure 3b). This observation convincingly demonstrates the key role of the PVDF-HFP coating in minimizing dendrite formation, thereby improving the stability and safety of AZIBs. This further confirms the excellent performance and potential value of the P-Zn anode for AZIB applications.

To further illustrate the excellent performance of this coating, the bare Zn or P-Zn electrode was used as the anode and matched with the MnO_2 cathode to assemble the full cells (Zn||MnO_2 or P-Zn||MnO_2) for electrochemical testing. Figure 4a presents the Cyclic Voltammetry (CV) curves for the Zn||MnO_2 and P-Zn||MnO_2 full cells, recorded at a scan rate of 0.1 mV s^{-1} over a voltage window of 0.8 to 1.8 V. Both cells display two sets of redox peaks, which correspond to the sequential redox reactions involving the Mn^{4+}/Mn^{3+} transition [37]. Figure 4b compares the impedance of Zn||MnO_2 and P-Zn||MnO_2 full cells. The resistance of the P-Zn electrode is reduced by almost 50%. There are two reasons for this: one is the inevitable formation of ZnO on the bare Zn anode surface, which increases the resistance; the other is the 3D structure of the PVDF-HFP coating, which provides more channels for the migration of Zn^{2+}, promoting homogeneous deposition, and increasing the nucleation sites, thus reducing the resistance [38].
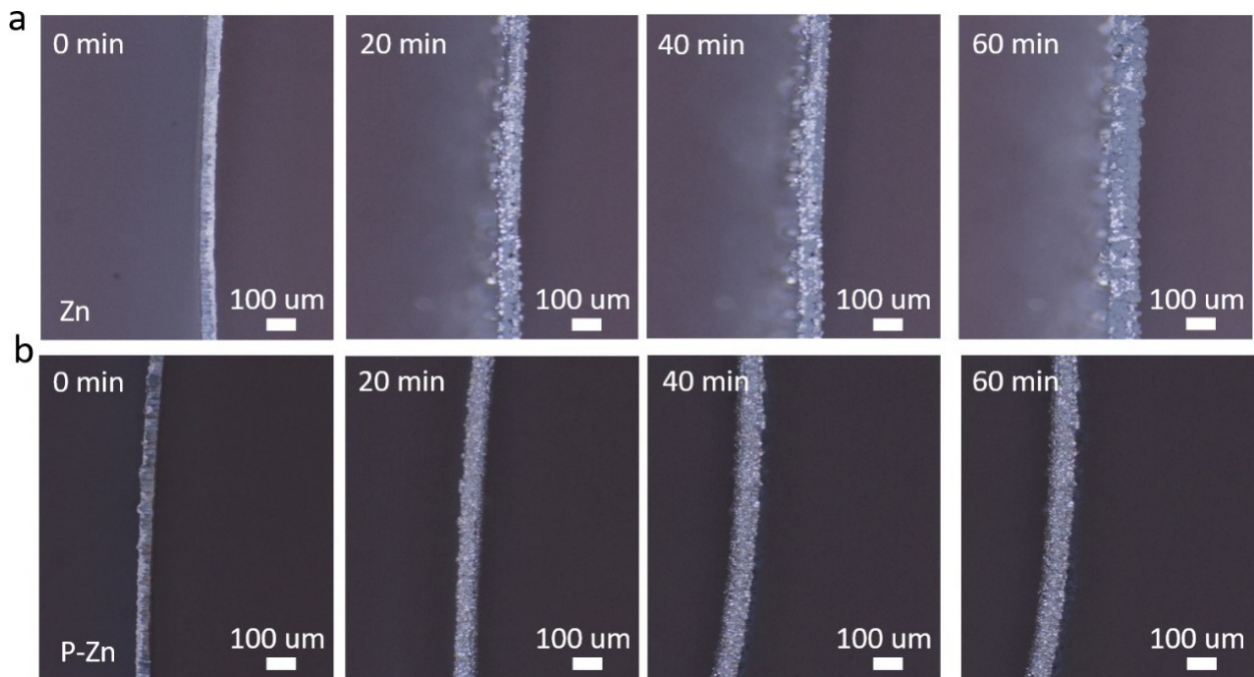
Figure 3. The dendrite growth behavior on (**a**) bare Zn and (**b**) P-Zn electrodes operating at 10 mA cm^{-2} for 60 min were observed using in situ optical microscopy.
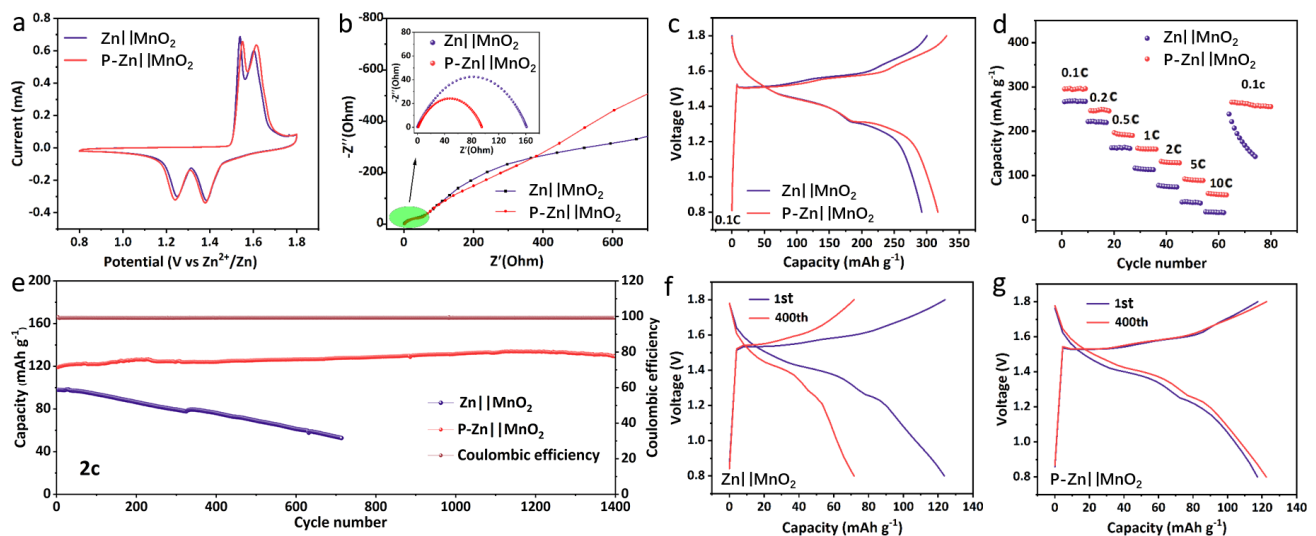

Figure 4. Electrochemical performance analysis of full cells utilizing either bare Zn or P-Zn electrodes as anodes, with MnO$_2$ serving as the cathode. (**a**) CV curves. (**b**) Nyquist impedance plots obtained prior to cycling. (**c**) Galvanostatic charge–discharge profiles at a current rate of 0.1C. (**d**) Rate capability assessment. (**e**) Long-term cycling stability evaluated at 2C. Galvanostatic charge–discharge profiles of (**f**) Zn||MnO$_2$ and (**g**) P-Zn||MnO$_2$ at 2C for the 1st and 400th cycle.

Figure 4c presents a comparison of the initial charge–discharge profiles for the Zn||MnO$_2$ and P-Zn||MnO$_2$ cells at a rate of 0.1C (where 1C equals 308 mAh g^{-1}). The specific capacity of the P-Zn||MnO$_2$ cell is about 320 mAh g^{-1}. On the other hand, although the Zn||MnO$_2$ cell shows comparable charge–discharge behavior, its specific capacity is reduced, achieving only 287 mAh g^{-1}. The rate of performance of Zn||MnO$_2$ and P-Zn||MnO$_2$ full cells are compared in Figure 4d. At 0.1, 0.2, 0.5, 1, 2, 5, and 10C, the P-Zn||MnO$_2$ cell achieved specific capacities of 300, 253, 203, 167, 134, 95, and 82 mAh g^{-1}, respectively, which were superior to those of the Zn||MnO$_2$ cell in each case, demonstrating an excellent rate capability.

Figure 4e compares the long-cycle stability of $Zn||MnO_2$ and $P-Zn||MnO_2$ full cells at 2 C. The capacity of the $Zn||MnO_2$ cells gradually decreased during cycling, and the capacity of retention was 50% after 700 cycles. This degradation can be attributed to the self-corrosion and dendrite generation of the bare Zn electrode during the cycling process, which ultimately led to the short circuit. In contrast, the capacity retention of the $P-Zn||MnO_2$ cell was 100% after 1400 cycles. The PVDF-HFP coating minimizes electrode–electrolyte interactions, thereby reducing side reactions and enhancing the reversibility of Zn^{2+}/Zn stripping/plating [26,34]. This improvement in interface stability contributes to the enhanced cycling performance of the $P-Zn||MnO_2$ cell. The increased capacity during cycling can be attributed to the activation of MnO_2 in the electrolyte and the nanoscale transformation of manganese ions, which continuously generate nanoscale MnO_2 at the cathode [39]. In addition, the charge–discharge profiles of two full cells after 400 cycles were selected, as shown in Figure 4f,g. It is clear that the $Zn||MnO_2$ cell rapidly lost 50% of its capacity after 400 cycles, while the $P-Zn||MnO_2$ cell maintained a stable charge–discharge profile. All these test results demonstrate the potential of PVDF-HFP coatings to enhance the performance of AZIBs. Figure S5 shows the long-term cycling performance of the $P-Zn25||MnO_2$ and $P-Zn75||MnO_2$ cells at 2C. The $P-Zn25||MnO_2$ cell demonstrated capacity retention of 37% after 600 cycles (Figure S5a), while the $P-Zn75||MnO_2$ cell maintained only 9% capacity retention after 1400 cycles (Figure S5b). In the comparison of the long cycling performance of PVDF coating samples in Figures 4e and S5, $P-Zn||MnO_2$ exhibits the best stability. The low content of PVDF-HFP in P-Zn25 does not encapsulate Zn well to inhibit the occurrence of the side reaction, while the high content of PVDF-HFP in P-Zn75 is too dense for the transport of Zn^{2+}.

In order to reveal the growth of dendrites during the cycling process, the surface morphology of bare Zn and P-Zn electrodes was observed using FESEM after 400 cycles at 2C. The surface of the bare Zn electrode displayed noticeable irregularities in the deposition layers, as shown in Figure 5a,b. Lamellar dendritic growth resulted in poor cycling stability and slow redox kinetics. In contrast, on the surface of the P-Zn electrode, the deposited layer was more uniform (Figure 5c,d) and remained smooth and dense without dendritic growth, which effectively improved the cycling stability of $P-Zn||MnO_2$ cells. The cycling stability of the $P-Zn||MnO_2$ cell was effectively improved.
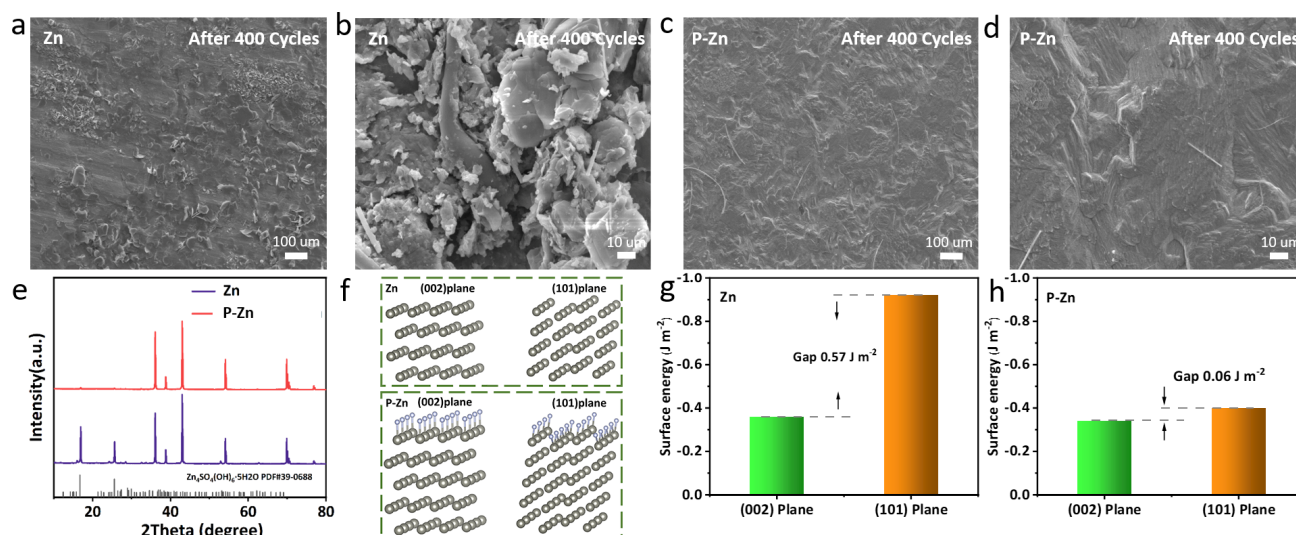

Figure 5. FESEM images of Zn (**a**,**b**) and P-Zn (**c**,**d**) electrodes; (**e**) XRD patterns of Zn and P-Zn electrodes. (**f**) The crystal models of DFT calculation. Surface energies of Zn atoms adsorbed on bare Zn (**g**), P-Zn (**h**) (002), and (101) planes.

The XRD patterns of the two electrodes after 400 cycles are shown in Figure 5e. It was clear that the bare Zn electrode showed obvious sulfate corrosion peaks, which was

the consequence of destroying the stability of the anode [31]. In contrast, the XRD pattern of the P-Zn electrode was basically unchanged, further proving its corrosion resistance during the cycling process. This can primarily be attributed to the strong hydrophobic nature of the PVDF-HFP coating, which effectively minimizes direct interactions between the P-Zn anode and the electrolyte. As a result, this reduces both hydrogen evolution and the risk of corrosion. The contact angle tests of bare Zn and P-Zn electrodes are shown in Figures S6 and S7. The results show that the contact angle of the PVDF- HFP coated surface was reduced by 20 degrees compared with that of the bare Zn surface, indicating that the coating had a favorable hydrophobicity performance.

In order to deeply understand the effect of the PVDF-HFP coating on Zn^{2+} stripping/plating, using the Vienna Abinitio Simulation Package (VASP) to carry out the surface energy of the Zn and P-Zn (002) and (101) planes by DFT calculations, the crystal models of Zn and P-Zn are shown in Figure 5f [11,40]. For the bare Zn anode (Figure 5g), the surface energy on the (002) plane was -0.36 J m^{-2}, which is significantly larger than that on the (101) plane (-0.92 J m^{-2}, the gap of plans: 0.57 J m^{-2}), indicating the preferential deposition of Zn atoms on the (101) plane [28]. This preferential deposition is the main reason for the inhomogeneous deposition of Zn^{2+} and the generation of dendrites. On the contrary, after coating the PVDF-HFP coating, the difference in surface energies between the P-Zn anode (002) and (101) planes was not significant (the gap of plans: 0.06 J m^{-2}, Figure 5h), which effectively suppressed the inhomogeneous deposition of Zn^{2+}, and thus, favored the reduction in Zn dendrite growth.

Figure 6a vividly illustrates the side reactions and dendrite growth that occur in bare Zn during the cell operation. Firstly, Zn^{2+} was unevenly deposited on the bare Zn surface during plating. Due to the concentration of the electric field and concentration polarization, Zn^{2+} tends to preferentially accumulate on these protrusions. This phenomenon leads to the uneven nucleation of Zn^{2+}, fostering dendrite growth [41]. Secondly, the contact of bare Zn with the aqueous solution during the stripping/plating process led to hydrogen evolution. The precipitation of H_2 results in localized pH increases and the accumulation of by-products such as ZSH [42], which contribute to the degradation of the cell's performance over extended cycling and leads to the reduced lifespan of the cells over prolonged usage [43]. In the case of Zn^{2+} stripping and plating on the P-Zn electrode, as shown in Figure 6b, it exhibits a more stable performance over cycles. This PVDF-HFP coating has a dense structure, which reduces the surface energy gap between the (002) and (101) surfaces (Figure 5g,h) and guides the homogeneous Zn^{2+} deposition. After plating, the P-Zn electrode remained smooth, and no dendrites were detected (Figure 3b), indicating that the PVDF-HFP coating favored the homogenization of the nuclear sites.
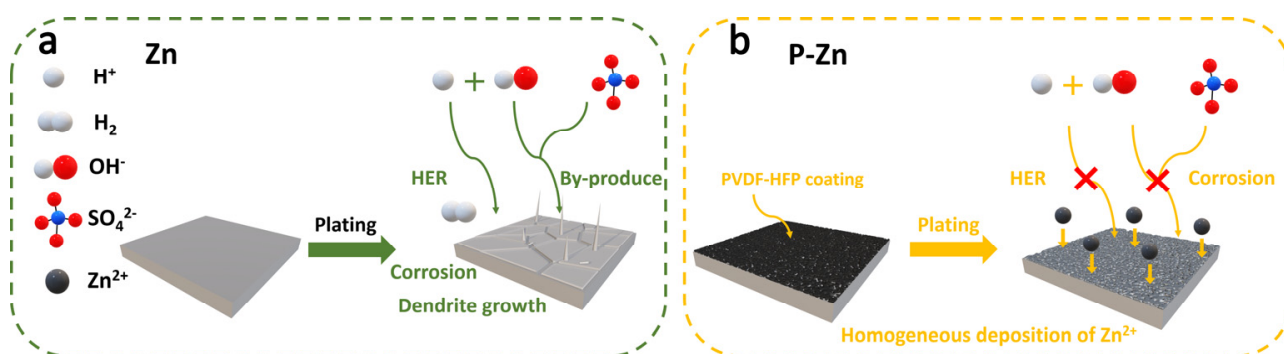

Figure 6. The behavior of Zn^{2+} stripping and plating on bare Zn (**a**) and P-Zn (**b**) electrodes in the $ZnSO_4$ aqueous electrolyte.

4. Conclusions

In this study, we used an economical and simple blade-coating technique to successfully apply a uniform and dense PVDF-HFP coating on the Zn metal surface. This organic coating, with its compact microstructure, effectively isolates the Zn metal from the aqueous

electrolyte, significantly reducing self-corrosion and hydrogen evolution. Notably, the unique porous structure of the coating not only improves the transport efficiency of Zn^{2+} but also provides a large number of active sites. DFT calculations show that the PVDF-HFP coating facilitates the homogeneous deposition of Zn^{2+} and effectively inhibits the growth of dendrites, which significantly improves the overall stability and lifespan of the AZIBs. P-Zn as an anode and MnO_2 as an anode are assembled as full cells, and their capacity retention is 100% after 1400 cycles at 2C. The P-Zn materials reported in this study are promising for the preparation of highly stable AZIBs.

Supplementary Materials: The following supporting information can be downloaded at https://www.mdpi.com/article/10.3390/batteries10120420/s1. Figure S1: FESEM image of the thickness of P-Zn; Figure S2: FESEM image of P-Zn25; Figure S3: FESEM image of P-Zn75; Figure S4: FESEM image of P-Zn25 after 24 h of immersion; Figure S5: Long-term cycling performance of full cells using the bare P-Zn25 (a) or P-Zn75 (b) electrode as the anode and MnO_2 as the cathode at 2 C; Figure S6: Contact angle of P-Zn anode electrode material; Figure S7: Contact angle of bare Zn anode electrode material. References [44–47] are cited in the supplementary materials.

Author Contributions: Conceptualization, F.L. and C.W.; methodology, F.L. and H.Z.; software, F.L.; validation, F.L. and C.W.; formal analysis, F.L.; investigation, X.L. and B.X.; resources, X.L. and C.W.; data curation, F.L.; writing—original draft preparation, F.L.; writing—review and editing, B.X. and C.W.; visualization, F.L.; supervision, C.W.; project administration, C.W.; funding acquisition, C.W. All authors have read and agreed to the published version of the manuscript.

Data Availability Statement: The original contributions presented in the study are included in the article/Supplementary Materials, further inquiries can be directed to the corresponding author.

Conflicts of Interest: The authors declare no conflicts of interest.

References

1. Jia, X.; Liu, C.; Neale, Z.G.; Yang, J.; Cao, G. Active Materials for Aqueous Zinc Ion Batteries: Synthesis, Crystal Structure, Morphology, and Electrochemistry. *Chem. Rev.* **2020**, *120*, 7795–7866. [CrossRef] [PubMed]
2. Chen, H.; Wang, C.; Wu, H.; Li, L.; Xing, Y.; Zhang, C.; Long, X. Host-Guest-Induced Electronic State Triggers Two-Electron Oxygen Reduction Electrocatalysis. *Nat. Commun.* **2024**, *15*, 9222. [CrossRef] [PubMed]
3. Gao, L.; Li, F.; Jin, X.; Li, Z.; Wang, C. Stabilizing 4.6 V $LiCoO_2$ via Surface-to-Bulk Titanium Modification. *Adv. Funct. Mater.* **2024**, 2416338. [CrossRef]
4. Wang, B.; Xu, H.; Hao, J.; Du, J.; Wu, C.; Ma, Z.; Qin, W. Mini-Review on the Regulation of Electrolyte Solvation Structure for Aqueous Zinc Ion Batteries. *Batteries* **2023**, *9*, 73. [CrossRef]
5. Wang, T.; Li, C.; Xie, X.; Lu, B.; He, Z.; Liang, S.; Zhou, J. Anode Materials for Aqueous Zinc Ion Batteries: Mechanisms, Properties, and Perspectives. *ACS Nano* **2020**, *14*, 16321–16347. [CrossRef] [PubMed]
6. Xie, C.; Li, Y.; Wang, Q.; Sun, D.; Tang, Y.; Wang, H. Issues and Solutions Toward Zinc Anode in Aqueous Zinc-Ion Batteries: A Mini Review. *Carbon Energy* **2020**, *2*, 540–560. [CrossRef]
7. Zheng, J.; Zhao, Q.; Tang, T.; Yin, J.; Quilty, C.D.; Renderos, G.D.; Liu, X.; Deng, Y.; Wang, L.; Bock, D.C.; et al. Reversible Epitaxial Electrodeposition of Metals in Battery Anodes. *Science* **2019**, *366*, 645–648. [CrossRef]
8. Shen, Q.; Wang, Y.; Han, G.; Li, X.; Yuan, T.; Sun, H.; Gong, Y.; Chen, T. Recent Progress in Electrolyte Additives for Highly Reversible Zinc Anodes in Aqueous Zinc Batteries. *Batteries* **2023**, *9*, 284. [CrossRef]
9. Zhang, Y.; Wei, C.; Wu, M.-X.; Wang, Y.; Jiang, H.; Zhou, G.; Tang, X.; Liu, X. A High-Performance COF-Based Aqueous Zinc-Bromine Battery. *Chem. Eng. J.* **2023**, *451*, 138915. [CrossRef]
10. Huang, J.; He, B.; Zhi, J.; Chen, P.; Wang, C.; Chen, H.; Zhao, X.S. Formation and Conversion of Hydrate Zinc Sulfate Hydroxide in Aqueous Zn/MnO_2 Batteries. *J. Power Sources* **2024**, *623*, 235409. [CrossRef]
11. Wang, R.; Xin, S.; Chao, D.; Liu, Z.; Wan, J.; Xiong, P.; Luo, Q.; Hua, K.; Hao, J.; Zhang, C. Fast and Regulated Zinc Deposition in a Semiconductor Substrate toward High-Performance Aqueous Rechargeable Batteries. *Adv. Funct. Mater.* **2022**, *32*, 2207751. [CrossRef]
12. Liang, P.; Yi, J.; Liu, X.; Wu, K.; Wang, Z.; Cui, J.; Liu, Y.; Wang, Y.; Xia, Y.; Zhang, J. Highly Reversible Zn Anode Enabled by Controllable Formation of Nucleation Sites for Zn-Based Batteries. *Adv. Funct. Mater.* **2020**, *30*, 1908528. [CrossRef]
13. He, P.; Huang, J. Chemical Passivation Stabilizes Zn Anode. *Adv. Mater.* **2022**, *34*, 2109872. [CrossRef] [PubMed]
14. Thieu, N.A.; Li, W.; Chen, X.; Hu, S.; Tian, H.; Tran, H.N.N.; Li, W.; Reed, D.M.; Li, X.; Liu, X. An Overview of Challenges and Strategies for Stabilizing Zinc Anodes in Aqueous Rechargeable Zn-Ion Batteries. *Batteries* **2023**, *9*, 41. [CrossRef]

15. Zeng, Y.; Zhang, X.; Qin, R.; Liu, X.; Fang, P.; Zheng, D.; Tong, Y.; Lu, X. Dendrite-Free Zinc Deposition Induced by Multifunctional CNT Frameworks for Stable Flexible Zn-Ion Batteries. *Adv. Mater.* **2019**, *31*, 1903675. [CrossRef]

16. Li, C.; Shi, X.; Liang, S.; Ma, X.; Han, M.; Wu, X.; Zhou, J. Spatially Homogeneous Copper Foam as Surface Dendrite-Free Host for Zinc Metal Anode. *Chem. Eng. J.* **2020**, *379*, 122248. [CrossRef]

17. Guo, S.; Qin, L.; Zhang, T.; Zhou, M.; Zhou, J.; Fang, G.; Liang, S. Fundamentals and Perspectives of Electrolyte Additives for Aqueous Zinc-Ion Batteries. *Energy Storage Mater.* **2021**, *34*, 545–562. [CrossRef]

18. Blanc, L.E.; Kundu, D.; Nazar, L.F. Scientific Challenges for the Implementation of Zn-Ion Batteries. *Joule* **2020**, *4*, 771–799. [CrossRef]

19. De Cachinho Cordeiro, I.; Li, A.; Lin, B.; Ma, D.; Xu, L.; Eh, A.; Wang, W. Solid Polymer Electrolytes for Zinc-Ion Batteries. *Batteries* **2023**, *9*, 343. [CrossRef]

20. Xia, A.; Pu, X.; Tao, Y.; Liu, H.; Wang, Y. Graphene Oxide Spontaneous Reduction and Self-Assembly on the Zinc Metal Surface Enabling a Dendrite-Free Anode for Long-Life Zinc Rechargeable Aqueous Batteries. *Appl. Surf. Sci.* **2019**, *481*, 852–859. [CrossRef]

21. Dong, L.; Yang, W.; Yang, W.; Tian, H.; Huang, Y.; Wang, X.; Xu, C.; Wang, C.; Kang, F.; Wang, G. Flexible and Conductive Scaffold-Stabilized Zinc Metal Anodes for Ultralong-Life Zinc-Ion Batteries and Zinc-Ion Hybrid Capacitors. *Chem. Eng. J.* **2020**, *384*, 123355. [CrossRef]

22. Wang, S.-B.; Ran, Q.; Yao, R.-Q.; Shi, H.; Wen, Z.; Zhao, M.; Lang, X.-Y.; Jiang, Q. Lamella-Nanostructured Eutectic Zinc–Aluminum Alloys as Reversible and Dendrite-Free Anodes for Aqueous Rechargeable Batteries. *Nat. Commun.* **2020**, *11*, 1634. [CrossRef] [PubMed]

23. Liu, B.; Wang, S.; Wang, Z.; Lei, H.; Chen, Z.; Mai, W. Novel 3D Nanoporous Zn-Cu Alloy as Long-Life Anode toward High-Voltage Double Electrolyte Aqueous Zinc-Ion Batteries. *Small* **2020**, *16*, 2001323. [CrossRef] [PubMed]

24. Cui, Y.; Zhao, Q.; Wu, X.; Chen, X.; Yang, J.; Wang, Y.; Qin, R.; Ding, S.; Song, Y.; Wu, J.; et al. An Interface-Bridged Organic-Inorganic Layer that Suppresses Dendrite Formation and Side Reactions for Ultra-Long-Life Aqueous Zinc Metal Anodes. *Angew. Chem. Int. Ed.* **2020**, *59*, 16594–16601. [CrossRef]

25. Zhou, Y.; Xie, S.; Li, Y.; Zheng, Z.; Dong, L. Sieve-Like Interface Built by ZnO Porous Sheets Towards Stable Zinc Anodes. *J. Colloid. Interf. Sci.* **2023**, *630*, 676–684. [CrossRef]

26. Lu, H.; Jin, Q.; Jiang, X.; Dang, Z.-M.; Zhang, D.; Jin, Y. Vertical Crystal Plane Matching Between AgZn$_3$ (002) and Zn (002) Achieving a Dendrite-Free Zinc Anode. *Small* **2022**, *18*, 2200131. [CrossRef]

27. He, H.; Tong, H.; Song, X.; Song, X.; Liu, J. Highly Stable Zn Metal Anodes Enabled by Atomic Layer Deposited Al$_2$O$_3$ Coating for Aqueous Zinc-Ion Batteries. *J. Mater. Chem. A* **2020**, *8*, 7836–7846. [CrossRef]

28. Zhao, Z.; Wang, R.; Peng, C.; Chen, W.; Wu, T.; Hu, B.; Weng, W.; Yao, Y.; Zeng, J.; Chen, Z.; et al. Horizontally Arranged Zinc Platelet Electrodeposits Modulated by Fluorinated Covalent Organic Framework Film for High-Rate and Durable Aqueous Zinc Ion Batteries. *Nat. Commun.* **2021**, *12*, 6606. [CrossRef]

29. Chen, P.; Yuan, X.; Xia, Y.; Zhang, Y.; Fu, L.; Liu, L.; Yu, N.; Huang, Q.; Wang, B.; Hu, X.; et al. An Artificial Polyacrylonitrile Coating Layer Confining Zinc Dendrite Growth for Highly Reversible Aqueous Zinc-Based Batteries. *Adv. Sci.* **2021**, *8*, 2100309. [CrossRef]

30. Zhao, Z.; Zhao, J.; Hu, Z.; Li, J.; Li, J.; Zhang, Y.; Wang, C.; Cui, G. Long-Life and Deeply Rechargeable Aqueous Zn Anodes Enabled by a Multifunctional Brightener-Inspired Interphase. *Energy Environ. Sci.* **2019**, *12*, 1938–1949. [CrossRef]

31. Deng, D.; Fu, K.; Yu, R.; Zhu, J.; Cai, H.; Zhang, X.; Wu, J.; Luo, W.; Mai, L. Ion Tunnel Matrix Initiated Oriented Attachment for Highly Utilized Zn Anodes. *Adv. Mater.* **2023**, *35*, 2302353. [CrossRef] [PubMed]

32. Baghodrat, M.; Zampardi, G.; Glenneberg, J.; La Mantia, F. Influence of the Thermal Treatment on the Structure and Cycle Life of Copper Hexacyanoferrate for Aqueous Zinc-Ion Batteries. *Batteries* **2023**, *9*, 170. [CrossRef]

33. Yin, H.; Liu, Y.; Zhu, Y.; Ye, F.; Xu, G.; Lin, M.; Kang, W. Bimetal-Initiated Concerted Zn Regulation Enabling Highly Stable Aqueous Zn-Ion Batteries. *Batteries* **2024**, *10*, 70. [CrossRef]

34. Feng, J.; Li, X.; Cui, X.; Zhao, H.; Xi, K.; Ding, S. Periodically Alternating Electric Field Layers Induces the Preferential Growth of Zn (002) Plane for Ultralow Overpotential Zinc-Ion Batteries. *Adv. Energy Mater.* **2023**, *13*, 2204092. [CrossRef]

35. Bao, S.; Tu, M.; Huang, H.; Wang, C.; Chen, Y.; Sun, B.; Xu, B. Heterogeneous Iron Oxide Nanoparticles Anchored on Carbon Nanotubes for High-Performance Lithium-Ion Storage and Fenton-Like Oxidation. *J. Colloid. Interf. Sci.* **2021**, *601*, 283–293. [CrossRef]

36. Liu, Y.; Chen, S.; Yuan, H.; Xiong, F.; Liu, Q.; An, Y.; Zhang, J.; Wu, L.; Sun, J.; Zhang, Y.-W.; et al. Achieving Highly Reversible Zinc Metal Anode via Surface Termination Chemistry. *Sci. Bull.* **2023**, *68*, 2993–3002. [CrossRef]

37. Chen, M.; Yang, M.; Zhou, W.; Tian, Q.; Han, X.; Chen, J.; Zhang, P. Oriented Zn Plating Guided by Aligned ZnO Hexagonal Columns Realizing Dendrite-Free Zn Metal Electrodes. *J. Colloid. Interf. Sci.* **2023**, *644*, 368–377. [CrossRef]

38. Jia, R.; Zhang, R.; Yu, L.; Kong, X.; Bao, S.; Tu, M.; Liu, X.; Xu, B. Engineering a Hierarchical Carbon Supported Magnetite Nanoparticles Composite from Metal Organic Framework and Graphene Oxide for Lithium-Ion Storage. *J. Colloid. Interf. Sci.* **2023**, *630*, 86–98. [CrossRef]

39. Liang, R.; Fu, J.; Deng, Y.-P.; Pei, Y.; Zhang, M.; Yu, A.; Chen, Z. Parasitic Electrodeposition in Zn-MnO$_2$ Batteries and Its Suppression for Prolonged Cyclability. *Energy Storage Mater.* **2021**, *36*, 478–484. [CrossRef]

40. Zhao, R.; Dong, X.; Liang, P.; Li, H.; Zhang, T.; Zhou, W.; Wang, B.; Yang, Z.; Wang, X.; Wang, L.; et al. Prioritizing Hetero-Metallic Interfaces via Thermodynamics Inertia and Kinetics Zincophilia Metrics for Tough Zn-Based Aqueous Batteries. *Adv. Mater.* **2023**, *35*, 2209288. [CrossRef]

41. Yang, Y.; Liu, C.; Lv, Z.; Yang, H.; Zhang, Y.; Ye, M.; Chen, L.; Zhao, J.; Li, C.C. Synergistic Manipulation of Zn^{2+} Ion Flux and Desolvation Effect Enabled by Anodic Growth of a 3D ZnF_2 Matrix for Long-Lifespan and Dendrite-Free Zn Metal Anodes. *Adv. Mater.* **2021**, *33*, 2007388. [CrossRef] [PubMed]

42. Hao, J.; Li, X.; Zhang, S.; Yang, F.; Zeng, X.; Zhang, S.; Bo, G.; Wang, C.; Guo, Z. Designing Dendrite-Free Zinc Anodes for Advanced Aqueous Zinc Batteries. *Adv. Funct. Mater.* **2020**, *30*, 2001263. [CrossRef]

43. Li, Y.; Wu, P.; Zhong, W.; Xie, C.; Xie, Y.; Zhang, Q.; Sun, D.; Tang, Y.; Wang, H. A Progressive Nucleation Mechanism Enables Stable Zinc Stripping-Plating Behavior. *Energy Environ. Sci.* **2021**, *14*, 5563–5571. [CrossRef]

44. Hafner, J. Ab-initio simulations of materials using VASP: Density-functional theory and beyond. *J. Comput. Chem.* **2008**, *29*, 2044. [CrossRef]

45. Blochl, P.E. Projector augmented-wave method. *Phys. Rev. B* **1994**, *50*, 17953. [CrossRef]

46. Perdew, J.P.; Burke, K.; Ernzerhof, M. Generalized Gradient Approximation Made Simple. *Phys. Rev. Lett.* **1996**, *77*, 3865. [CrossRef]

47. Yang, H.G.; Sun, C.H.; Qiao, S.Z.; Zou, J.; Liu, G.; Smith, S.C.; Cheng, H.M.; Lu, G.Q. Anatase TiO_2 Single Crystals with a Large Percentage of Reactive Facets. *Nature* **2008**, *453*, 638. [CrossRef]